Supplementary Materials For

Crystalline Liquid-like Behavior: Surface Induced Secondary Grain Growth of Photovoltaic Perovskite Thin Film

Jingjing Xue[1]†, Rui Wang[1]†, Kai-Li Wang[2]†, Zhao-Kui Wang[1,2]*, Ilhan Yavuz[3], Yang Wang[4], Yingguo Yang[5], Xingyu Gao[5], Tianyi Huang[1], Selbi Nuryyeva[1], Jin-Wook Lee[1], Yu Duan[1], Liang-Sheng Liao[2]*, Richard Kaner[1] and Yang Yang[1]*

[1]Department of Materials Science and Engineering and California NanoSystems Institute, University of California Los Angeles, CA 90095, USA

[2]Institute of Functional Nano & Soft Materials (FUNSOM), Jiangsu Key Laboratory for Carbon-Based Functional Materials & Devices, Soochow University, Suzhou 215123, China

[3]Department of Physics, Marmara University, 34722, Ziverbey, Istanbul, Turkey.

[4]School of Chemistry and Chemical Engineering, Yangzhou University, Yangzhou 225002, China

[5]Shanghai Synchrotron Radiation Facility (SSRF), Zhangjiang Lab, Shanghai Advanced Research Institute, Chinese Academy of Sciences, Shanghai 201204, China

*Correspondence and requests for materials should be addressed to Z.K.W (email: zkwang@suda.edu.cn) or to L.S.L (email: lsliao@suda.edu.cn) or to Y.Y. (email: yangy@ucla.edu)

†These authors contributed equally to this work

Materials

Unless stated otherwise, solvents and chemicals were obtained commercially and used without further purification. N, N-dimethylformamide (DMF), dimethyl sulfoxide (DMSO), chlorobenzene (CB), isopropanol (IPA), toluene, water, oleyamine, n-butylamine, octylamine, PbI_2, HI, ethanol, diethyl ether and gold (Au) were obtained from Sigma-Aldrich Inc. 4-Isopropyl-4'-methyldiphenyliodonium Tetrakis(pentafluorophenyl)borate (TPFB) were obtained from TCI Inc. Formamidinium Iodide (FAI) was obtained from Great Cell. Methylammonium Bromide (MABr) and methylammonium chloride (MACl) were obtained from 1-Materials. PTAA was obtained from Xi'an Polymer Light Technology Corp. Tin Oxide (SnO_2) nanoparticle, $PbBr_2$, and CsI were obtained from Alfa-Aesar Inc. BAI, OCAI, and OLAI were home synthesized.

Method

Synthesis of Organic Ammoniums. n-Butyammonium Iodide (BAI) was synthesized by adding 8 mL 57 wt% aqueous hydriodic acid (HI) dropwise into 500 μL n-butylamine and ethanol. The mixture was vigorously stirred in an ice bath for 4 h under Ar flow, after which the solvent was removed using a rotary evaporator and the precipitate was dissolved in ethanol and recrystallized three times in diethyl ether. The BAI white powders obtained by the recrystallization process were then dried at 60 °C under vacuum overnight. Octylammonium Iodide (OCAI) and Oleylammonium Iodide (OLAI) were synthesized using a similar route as described above by replacing n-butylamine with octylamine, and oleylamine respectively. For OLAI, 12 h was needed for the complete reaction.

DFT Calculations. First-principles calculations were carried out using the VASP code[1,2]. The Perdew-Burke-Ernzerh (PBE)[3,4] generalized gradient approximation for the exchange-correlation functional was employed, with dispersion correction using Grimme's DFT-D3 scheme (with Becke-Johnson damping function)[5,6]. Projector-augmented-wave (PAW) pseudopotentials[7] were utilized for valence-core interactions. A sufficiently high kinetic energy cutoff of 400 eV was chosen for the plane wave expansion. Atomic positions and unit-cells were optimized using a conjugate gradient algorithm until all Hellman-Feynman forces are smaller than 0.02 eV/Å. Based on convergence assessment, a 4*4*4 Monkhorst-Pack k-point mesh[8] was chosen for Brillouin-zone sampling for bulk perovskites. For surfaces, k-point mesh is taken to be 1 for the direction of the surface. The surfaces were modeled by a periodic slab consisting of at least five atomic layers, separated by at least 25 Å of vacuum in the surface normal direction. During optimizations all layers were allowed to relax.

Device Fabrication. Perovskite solar cells were fabricated with the following structures: indium tin oxide (ITO)/SnO_2/$CsPbI_2Br$/PTAA/Au and ITO/SnO_2/$(FAPbI_3)_x(MAPbBr_3)_{1-x}$/PTAA/Au. The ITO glass was pre-cleaned in an ultrasonic bath of acetone and isopropanol and treated in ultraviolet ozone for 20 min. A thin layer (ca. 30 nm) of SnO_2 was spin-coated onto the ITO glass and baked at 180 °C for 60 min. SnO_2 was diluted in water (2 mg mL^{-1}). After cooling at room temperature, the glass/ITO/SnO_2 substrates were transferred into a nitrogen glove box. For the Cs-based perovskite, the solution was prepared by dissolving 0.5 mM PbI_2, 0.5 mM $PbBr_2$ and 1 mM CsI in 250 μL DMSO and 750 μL DMF. The perovskite solution was spin-coated on the preheated substrate (70 °C) at 2000 rpm for 35 s, to which 0.1 mL of IPA was dropped after 15 s. The spin-coated film was heat-treated at 65 °C for 1 min, 130 °C for 1 min, followed by 300 °C for 10 min.

For the FA-based perovskite, the PbI_2 solution was prepared by dissolving 1.4 mM PbI_2 into 1 mL DMF/DMSO mixed solvent (v/v 94/6). The FAI/MABr/MACl solution was prepared by dissolving 80 mg FAI, 5 mg MABr and 9 mg MACl into 1 ml IPA. The PbI_2 solution was spin-coated on the substrate at 1500 rpm for 30 s and annealed at 70 °C for 1 min. And the FAI/MABr/MACl solution was spin-coated on the substrate at 1800 rpm for 30 s, then the film was annealed outside the glove box at 150 °C for 10 min with 40% humidity. And then the BA/IPA, OCA/IPA or OLA/IPA solutions were drop cast at 4000 rpm. The films were dried at 100 °C for 5 min. The PTAA solution (30 mg/ml; in toluene with 10% TPFB for Cs-based perovskite, 40 mg/ml; in CB with 5% TPFB for FA-based perovskite) was spun onto the perovskite film as a hole conductor. The devices were completed by evaporating 100 nm gold in a vacuum chamber (base pressure, 5×10^{-4} Pa).

Device Characterization. *J–V* characteristics of photovoltaic cells were taken using a Keithley 2400 source measure unit under a simulated AM 1.5G spectrum, with an Oriel 9600 solar simulator. Typically, the devices were measured in reverse scan (1.3 V ⟶ 0 V, step 0.02 V, 100 mV/s) and forward scan (0 V ⟶ 1.3 V, step 0.02 V, 100 mV/s). All the devices were measured without pre-conditioning such as light-soaking and applied a bias voltage. Steady-state power conversion efficiency was calculated by measuring stabilized photocurrent density under a constant bias voltage. EQEs were measured using an integrated system (Enlitech, Taiwan) and a lock-in amplifier with a current preamplifier under short-circuit condition. For transient photovoltage (TPV) and current (TPC) measurements, a pulsed red dye laser (Rhodamine 6G, 590 nm) pumped by a nitrogen laser (LSI VSL-337ND-S) was used as the perturbation source, with a pulse width of 4 ns and a repetition frequency of 10 Hz. The intensity of the perturbation laser pulse was controlled to maintain the amplitude of transient V_{OC} below 5 mV so that the perturbation assumption of excitation light holds. The voltages under open circuit and currents under short circuit conditions were measured over a 1 MΩ and a 50 Ω resistor and were recorded on a digital oscilloscope (Tektronix DPO 4104B).

Materials Characterization. UV-vis absorption spectra of the perovskite films were obtained using a U-4100 spectrophotometer (Hitachi) equipped with integrating sphere, in which monochromatic light was incident to the substrate side. X-ray diffraction (XRD) patterns of the films were recorded by X-ray diffractometer (PANalytical) with Cu kα radiation at a scan rate of 4°/min. Surface images of the films were acquired by scanning electron microscopy (SEM, Quanta 200 FEG.). GIWAXS test was performed at the BL14B1 beamline of China Shanghai Synchrotron Radiation Facility (SSRF). 2D GIWAXS patterns were obtained by a MarCCD 225 detector mounted vertically at around 256.401 mm from the sample with an exposure time of 50 s at a grazing incidence angle of 0.15°. The x-axis of GIWAXS patterns was represented by the diffraction vector with $q = 4\pi\sin(\theta)/\lambda$, where θ is half of the diffraction angle and λ is the wavelength of incident X-ray. XPS measurements were carried out on an XPS AXIS Ultra DLD (Kratos Analytical). An Al Kα (1,486.6 eV) X-ray was used as the excitation source. The contact angles of the grid lines were measured by a PSSOCA20 optical contact-measuring system. Time of Flight-Secondary Ion Mass Spectroscopy (ToF-SIMS) was measured by a TOF.SIMS 5 (ION TOF GmbH Germany, 225332). The dielectric spectra were tested by Precision Impedance Analyzer (Agilent 4294A).

Supplementary Note S1. Density Functional Theory Calculations of Driving Force of SISG

To model surface free energies, low-index planes including (100), (010), (001), (110), (101), (011) and (111) are considered based on the corresponding cleavages of the bulk perovskite. The following information contains details of the surface energy calculation specifically for the (100) slab. The parameter information related to other surfaces are given in Table S3. Due to presence of previous optimization calculations, for simplification we use $CsPbI_2Br$ as the perovskite slab that contains one organic ammonium molecule (denoted by M) per cell. Thus, the chemical formula of the slab is $Cs_nPb_nI_{2n+1}Br$ per unit cell. To calculate the surface free energy γ, we first define the cleavage energy of a clean surface as to be

$$\gamma^{clean} = \frac{1}{2A}[G^{slab,unrel}_{Cs_nPb_nI_{2n+1}Br} - n\mu_{Cs} - n\mu_{Pb} - (2n+1)\mu_I] \quad \text{Eq. S1}$$

where "unrel" denotes unrelaxed surfaces, μ_i is the chemical potential of component *i* and A is the surface area per unit cell. As there is enough bulk $CsPbI_2Br$ to act as a thermodynamic reservoir, the chemical potentials of Cs, Pb, I and Br have the following relationship under thermodynamic equilibrium:

$$\mu_{Cs} + \mu_{Pb} + 2\mu_I = g^{bulk}_{CsPbI_2Br} \quad \text{Eq. S2}$$

where $g^{bulk}_{CsPbI_2Br}$ is Gibbs free energy per formula unit of bulk $CsPbI_2Br$. Plugging in Eq. S2 into Eq. S1 we get:

$$\gamma^{clean} = \frac{1}{A}(G^{slab,unrel}_{Cs_nPb_nI_{2n+1}Br} - \mu_I - ng^{bulk}_{CsPbI_2Br}) \quad \text{Eq. S3}$$

We will assume that the chemical potentials of Cs, Pb and Br are invariant for M molecules with different chain length, which is reasonable since the interactions between M and Cs or Pb are very similar (and also less important) for different M molecules (as shown in the optimized geometries, the predominant difference in structures of the slab of different Ms is the chains). As a result, the chemical potential of I is also constant according to Eq. S2. The relaxation of surface free energy of the slab upon ammonium molecule absorptions are evaluated as

$$\gamma^{rel} = (G^{slab,rel}_{MCs_nPb_nI_{2n+1}Br} - G^{slab,unrel}_{MCs_nPb_nI_{2n+1}Br})/A \quad \text{Eq. S4}$$

Thus, the surface free energy is determined from

$$\gamma = \gamma^{clean} + \gamma^{rel} \quad \text{Eq. S5}$$

where γ^{clean} becomes the energy of the clean surface, and γ^{rel} is the relaxation energy at $T = 0$ K. As an approximation, we neglect the free energy contributions that arise predominantly from the change of adsorbate vibrational properties (e.g. zero-point energies and vibrational entropy) upon adsorption[9]. These contributions are supposed to be small since we are comparing the relative surface energies for the slabs adsorbing M molecules with different chain length. The calculated γ^{clean} for different planes of $CsPbI_2Br$ were summarized in Fig. S15. It was found that plane (110), (101), and (011) are highly unstable compared to plane (100) and (111). Since plane (100) and

(111) are dominant, we only considered these two planes when we compared the surface energy with and without organic ammoniums.

Supplementary Note S2 Phase-field Model for Simulating Grain Growth in Polycrystalline Materials

In the Phase-field model, randomly oriented phases can be described by a field variable ϕ that distinguishes phases (or grains). The phase-field equations that solve the grain growth can be written as[10]

$$\dot{\phi_n} = \gamma\mu(\nabla^2\phi_n + \frac{\pi^2}{\eta^2}(\phi_n - \frac{1}{2})) + \frac{\pi\sqrt{\phi_n(1-\phi_n)}}{\eta}v_n \qquad \text{Eq. S6}$$

where, n represents each randomly oriented phase, μ is the interface mobility, γ is the interface energy (related to surface free energy), η is the interfacial width, $v_n = \mu\Delta g$ is the velocity and Δg is the driving force. Grain-growth simulations are carried out using OpenPhase open source software[11].

To simulate grain growth in $CsPbI_2Br$ films without OLA and with OLA treatments, surface energies of only 100 and 111 slabs are taken into account (see **Supplementary Note S1**). The grain growth of polycrystalline film is modelled by a box with dimensions 100*100*20 $\square m^3$. To construct the initial microstructure for simulations, randomly oriented grains and grain boundaries are distributed by Voronoi tessellation. For both "without OLA" and "with OLA" cases, the initial microstructures of the films are taken to be identical, in order for a clear demonstration of the effect of OLA on grain growth. Numerical solutions of grain growth are performed that lasted for 20 ms. The resulting snapshots of the simulations are shown in Fig. S3. Prior to this, we provided an analytical 1D grain growth simulation based on Phase-field model to demonstrate the effect of the increasing driving force.

Supplementary Note S3 Calculation of Surface Free Energy from Contact Angle Measurement. Contact angle measurement was used to prove the existence of SISG of the organic ammonium-terminated perovskite. Based on the previous literature[12], two liquid (water and diiodomethane) with known surface energy were selected. The adhesion work is defined as:

$$W_a = \gamma_{SL} + \gamma_{LV} - \gamma_{SL} \quad \text{Eq. S7}$$

where γ_{SL}, γ_{LV} and γ_{SL} represent the surface free energy between solid-liquid, liquid-vapor and liquid-vapor, respectively. From Young's equation,

$$\gamma_{SV} = \gamma_{SL} + \gamma_{LV}\cos\theta \quad \text{Eq. S8}$$

By combining Eq. S6 and Eq. S7, we obtain the following:

$$W_a = \gamma_{LV}(1 + \cos\theta) \quad \text{Eq. S9}$$

In the meantime, the adhesion work can be represented by the polar part and the dispersion part.

$$W_a = 2\sqrt{\gamma_{SV}^d \gamma_{LV}^p} + 2\sqrt{\gamma_{SV}^p \gamma_{LV}^d} \quad \text{Eq. S10}$$

Where γ_{SV}^d and γ_{LV}^d represent the dispersion part of the surface free energy between solid-vapor and liquid-vapor, respectively. And γ_{SV}^p and γ_{LV}^p represent the polar part of the surface free energy between solid-vapor and liquid-vapor, respectively. After plugin Eq. S9 into Eq. S8, we get,

$$\gamma_{LV}(1 + \cos\theta) = 2\sqrt{\gamma_{SV}^d \gamma_{LV}^p} + 2\sqrt{\gamma_{SV}^p \gamma_{LV}^d} \quad \text{Eq. S11}$$

According to the contact we measured (Fig. S6), the surface free energy of $CsPbI_2Br$ with OLA treatment is 38.38 mN/m and the surface free energy of $CsPbI_2Br$ without treatment is 59.78 mN/m. The smaller surface energy is consistent with calculated DFT, which proved the existence of the driving force of SISG. The detailed parameters were summarized in Table S2.

Supplementary Note S4 Additional Device Optimization and Characterization.

4.1 Device Optimization

We first fabricated the devices based on BA, OCA and OLA. Fig. S17A and Table S4 present the best and average photovoltaic performance of the device. The statistical distribution of device performance of devices based on BA, OCA and OLA are shown in Fig. S17B. Notably, the average PCEs with SISG induced by organic ammoniums are much higher than that of the reference device (12.17%). More importantly, the average PCE of OLA treated device (16.23%) is higher than that of BA (13.55%) and OCA (14.44%), which is consistent with largest grain size produced by SISG (Fig. 2). Notably, as shown in Fig. S16, BA and OCA penetrated into the perovskite active layer probably in the form of 2D layered perovskite, which may not beneficial to charge transport. To maximize the role of SISG induced by OLA in photovoltaic performance, we also optimized annealing time and annealing temperature of the SISG process and the concentration of OLA, the detailed photovoltaic parameters of which are summarized in Table S5-S7. The highest optimized device performance was 16.58%.

4.2 Mobility Characterization

The device structures for electron-only and hole-only and corresponding *J-V* curves are shown in Fig. S18. The mobility (μ) is extrapolated from the *J-V* curves (n=2) by using space charge limited current (SCLC) method with an equation of $J = 9\varepsilon_0\varepsilon_r\mu V^2/8d^3$, where ε_0 (=8.8542×10^{-14} F/cm) is permittivity of free space, ε_r (=6.5), d is the thickness of perovskite layer and q is the elementary charge. The calculated defect densities and carrier mobilities in the reference and targeted devices are shown in Table S8. OLA-treated $CsPbI_2Br$ showed higher mobility than that of the reference.

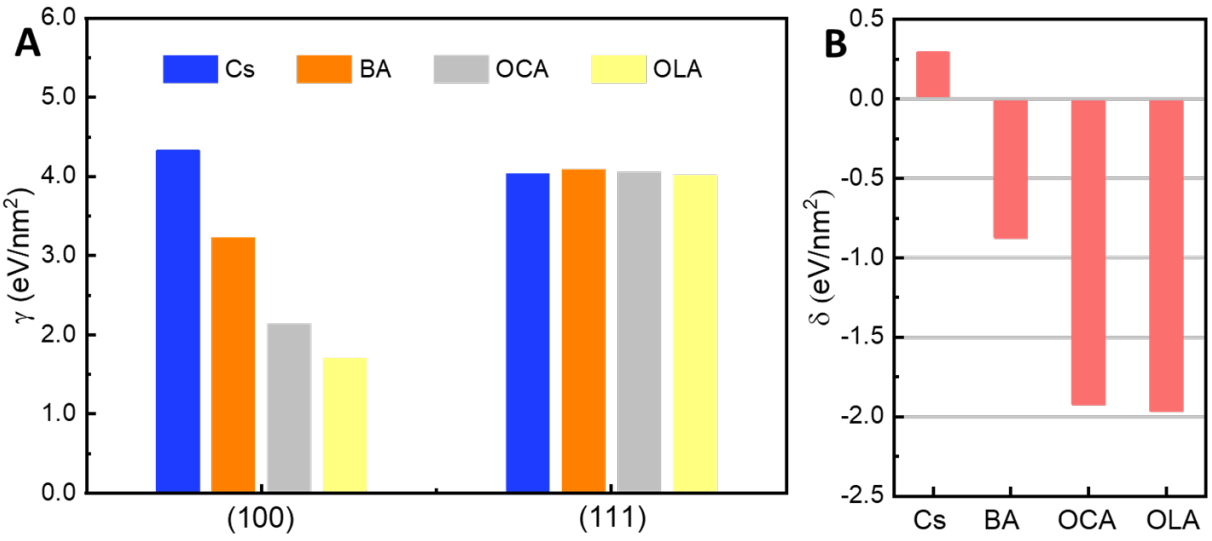

Fig. S1. (A) The calculated surface energy γ of plane (100) and (111) for $CsPbI_2Br$ slabs terminated with Cs, BA, OCA and OLA. (B) γ_{100}- γ_{111} for $CsPbI_2Br$ slabs terminated with Cs, BA, OCA and OLA.

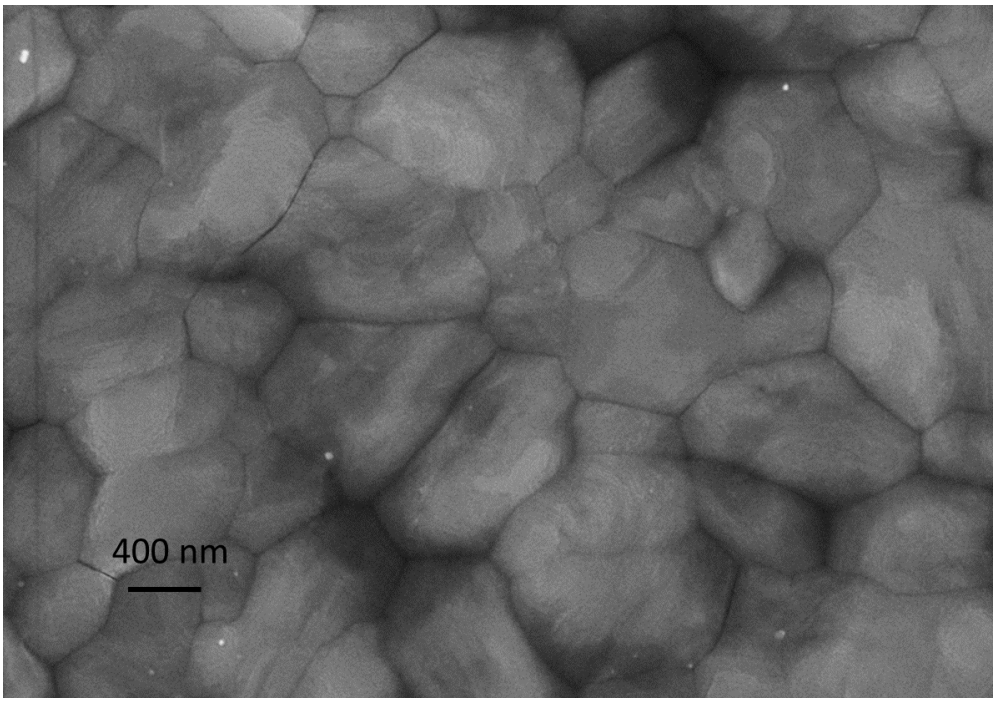

Fig. S2. SEM image of $CsPbI_2Br$ film without IPA treatment.

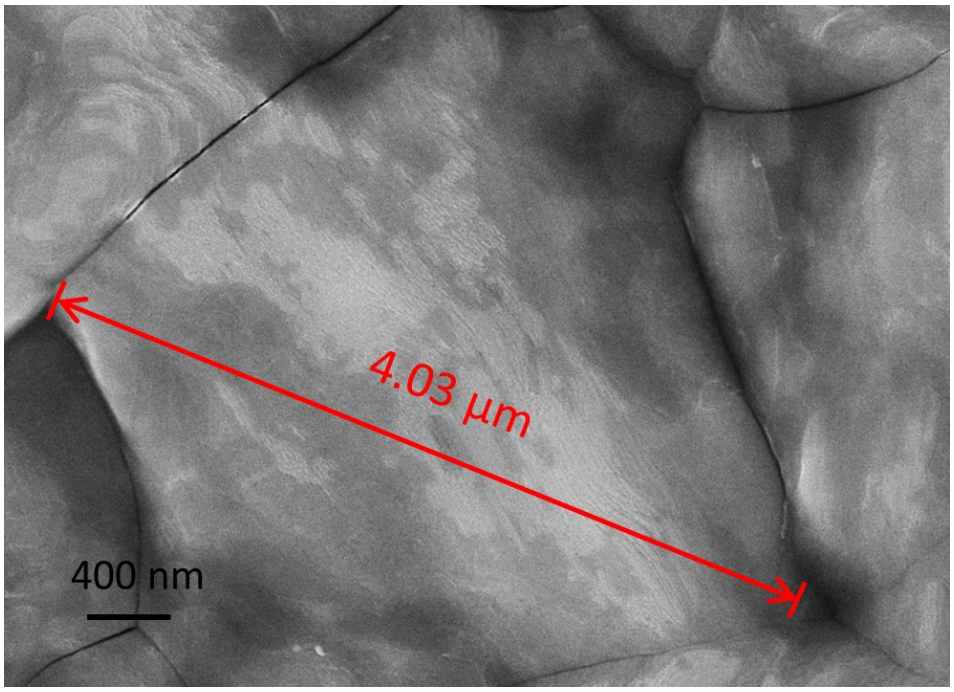

Fig. S3 SEM image of $CsPbI_2Br$ film with OLA treatment. The grain size is as large as 4 microns.

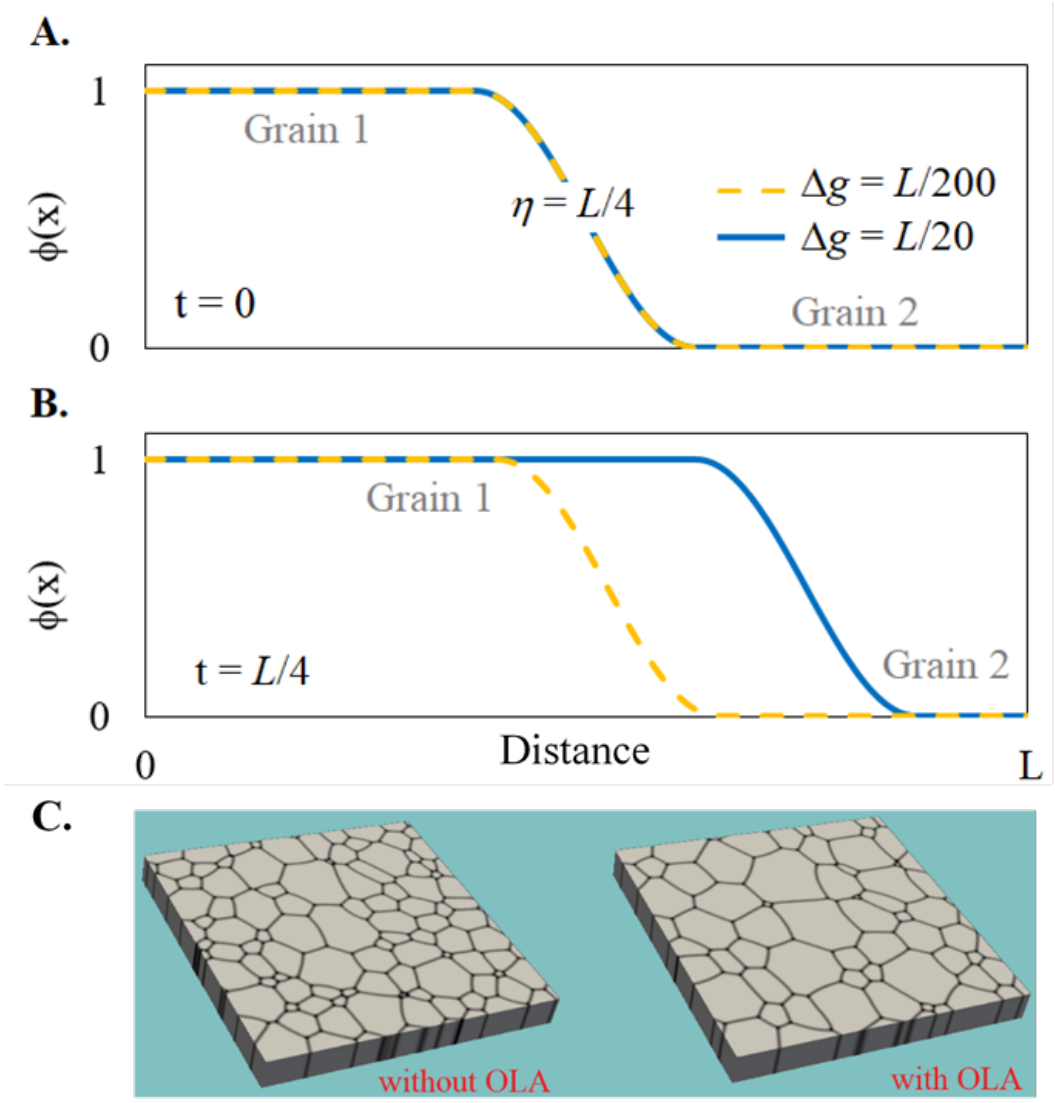

Fig. S4. (A)-(B) A demonstration of the Phase-field model: analytical calculations of a 1D grain growth with a smooth interface and two different driving forces, $\Delta g = L/200$ and $\Delta g = L/20$, where $\Delta g = v/\mu$ and μ is taken to be unity. (A) initial condition (t=0), (B) at a later time (t=L/4). L: total length, η: interface width. (C) Snapshots of a 3D simulated grain growth of $CsPbI_2Br$ films without OLA and with OLA treatments.

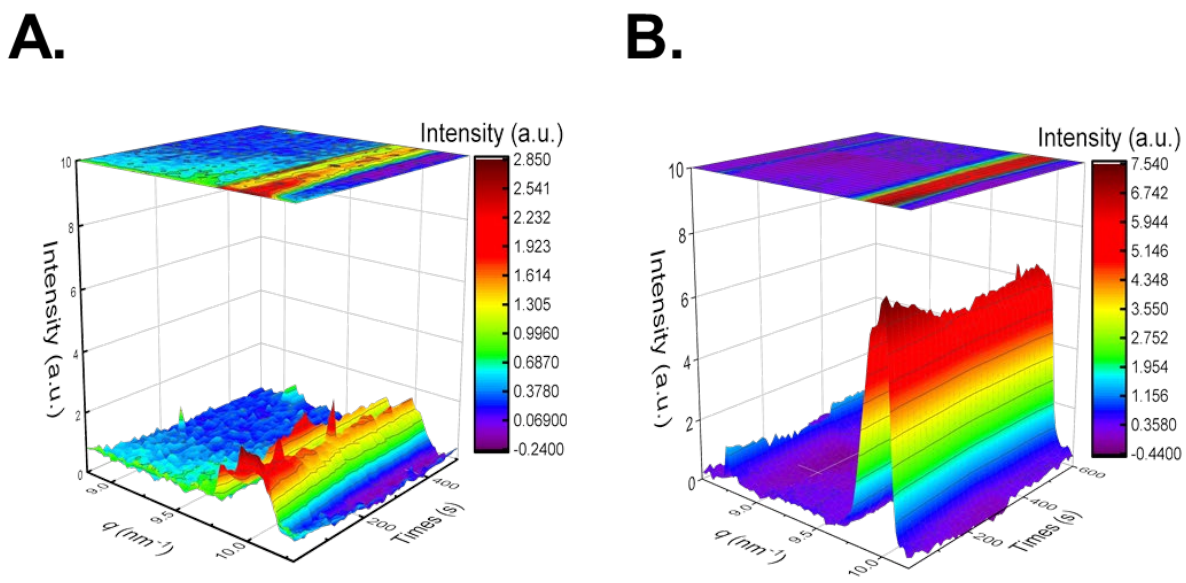

Fig. S5 3D in-situ GIWAXS patterns of $CsPbI_2Br$ films. (A) without OLA treatment; (B) with OLA treatment.

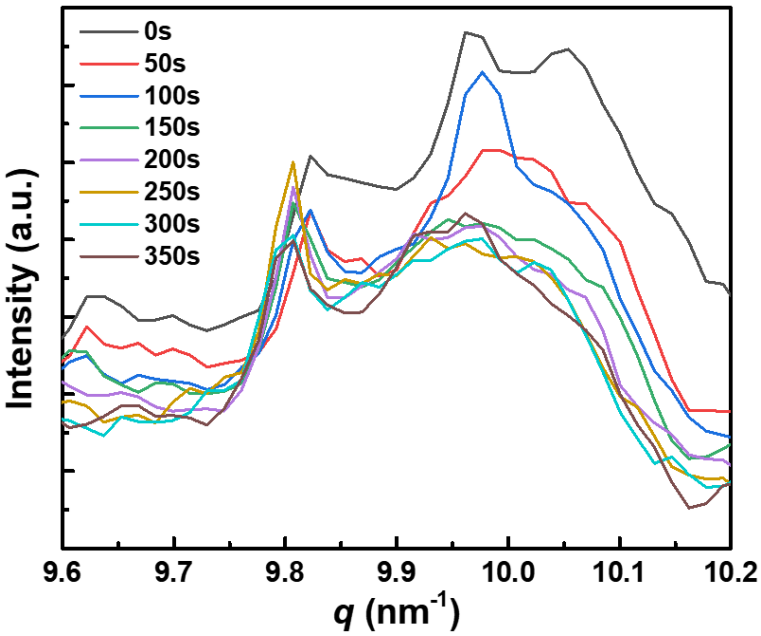

Fig. S6 Evolution of 1D GIWAXS patterns of $CsPbI_2Br$ films without OLA treatment.

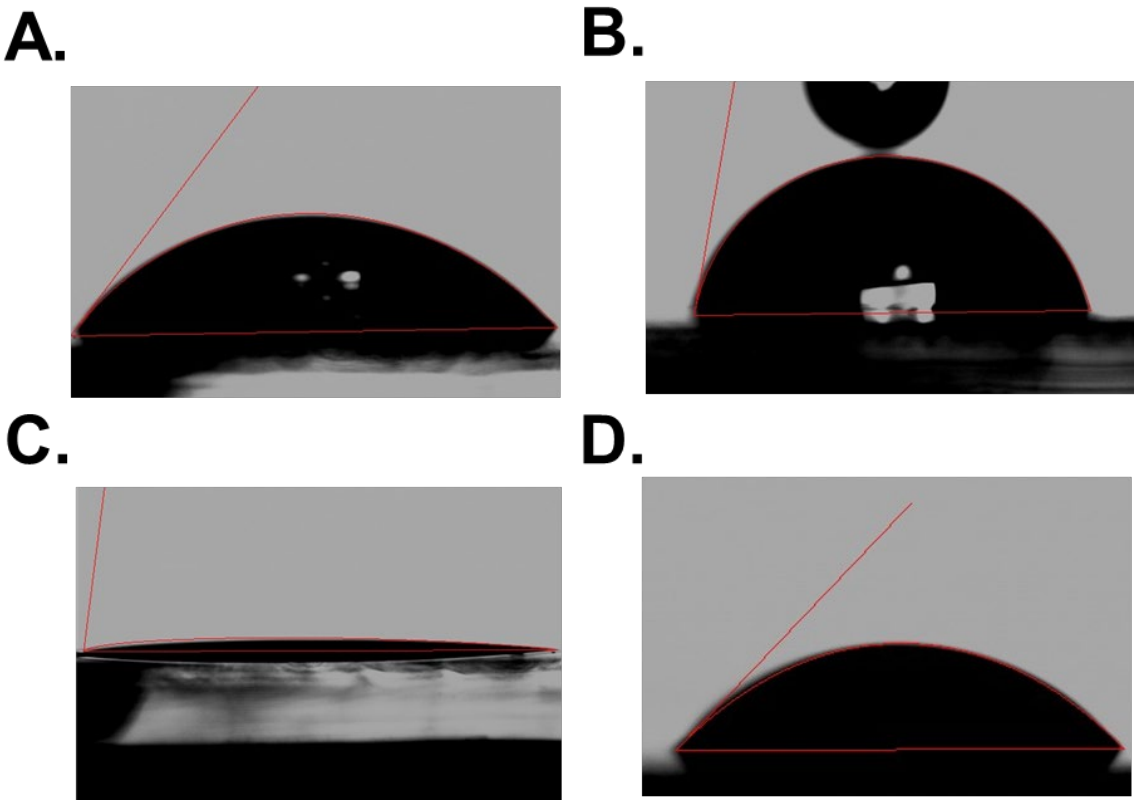

Fig. S7 Contact angles of H_2O with $CsPbI_2Br$ films. (A) without OLA treatment and (B) with OLA treatment on H_2O; and of diiodomethane (DIM) with $CsPbI_2Br$ films (C) without OLA treatment and (D) with OLA treatment.

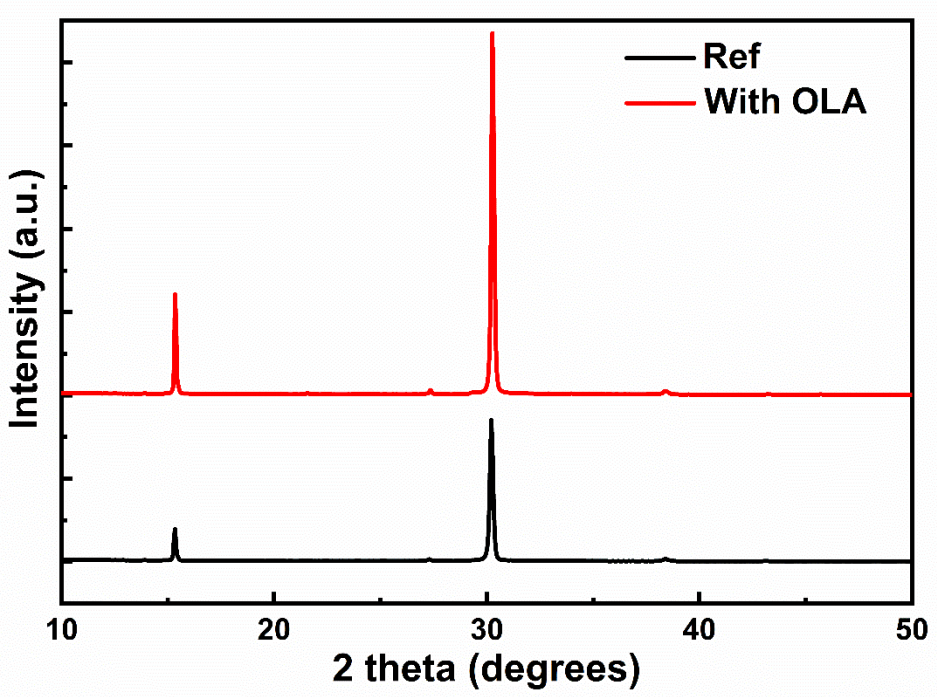

Fig. S8 XRD patterns of $CsPbI_2Br$ films with and without OLA treatment.

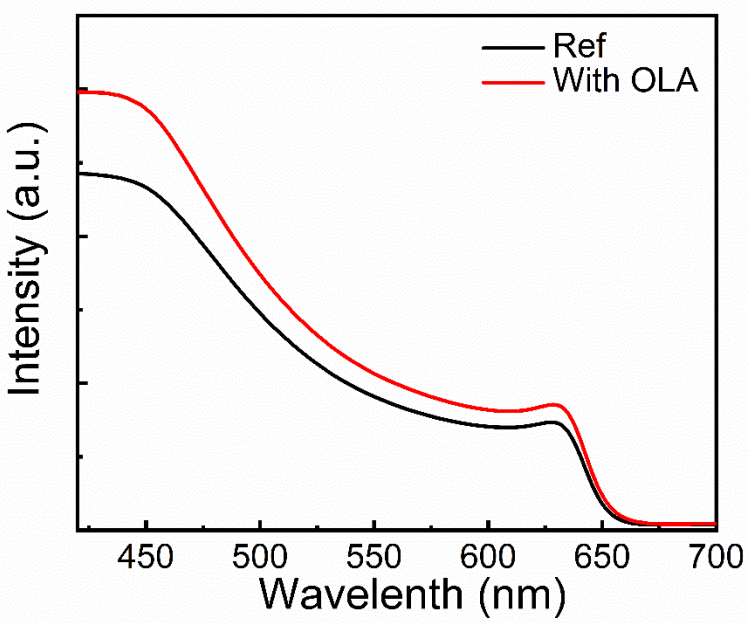

Fig. S9. UV-Vis spectra of $CsPbI_2Br$ films with and without OLA treatment.

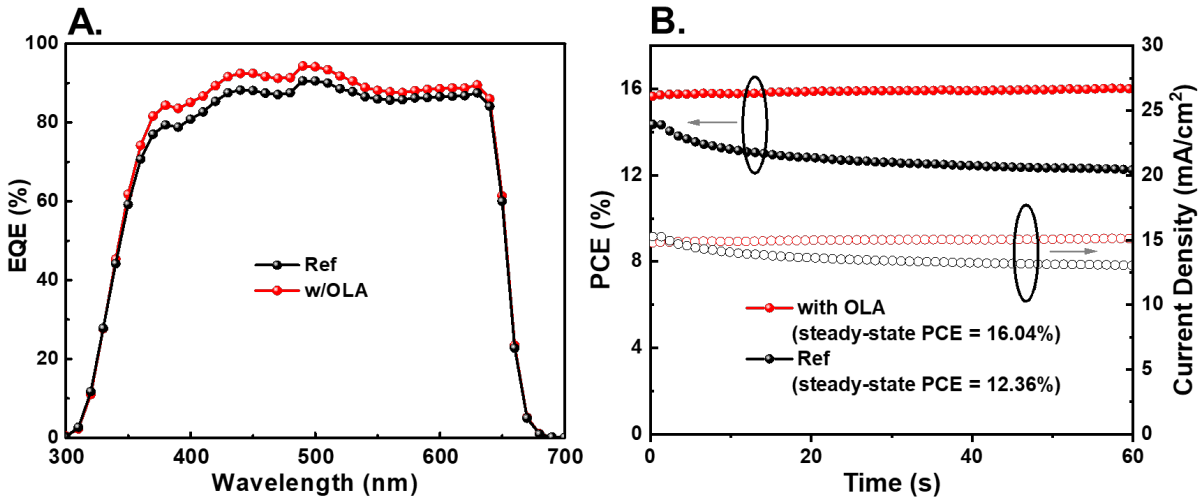

Fig. S10 (A) EQE curves of the devices with or without OLA treatment. (B) Stabilized maximum power output and the photocurrent density at maximum power point as a function of time for the best performing perovskite solar cells with or without OLA treatment, as shown in Figure 4A, recorded under simulated one-sun AM1.5G illumination.

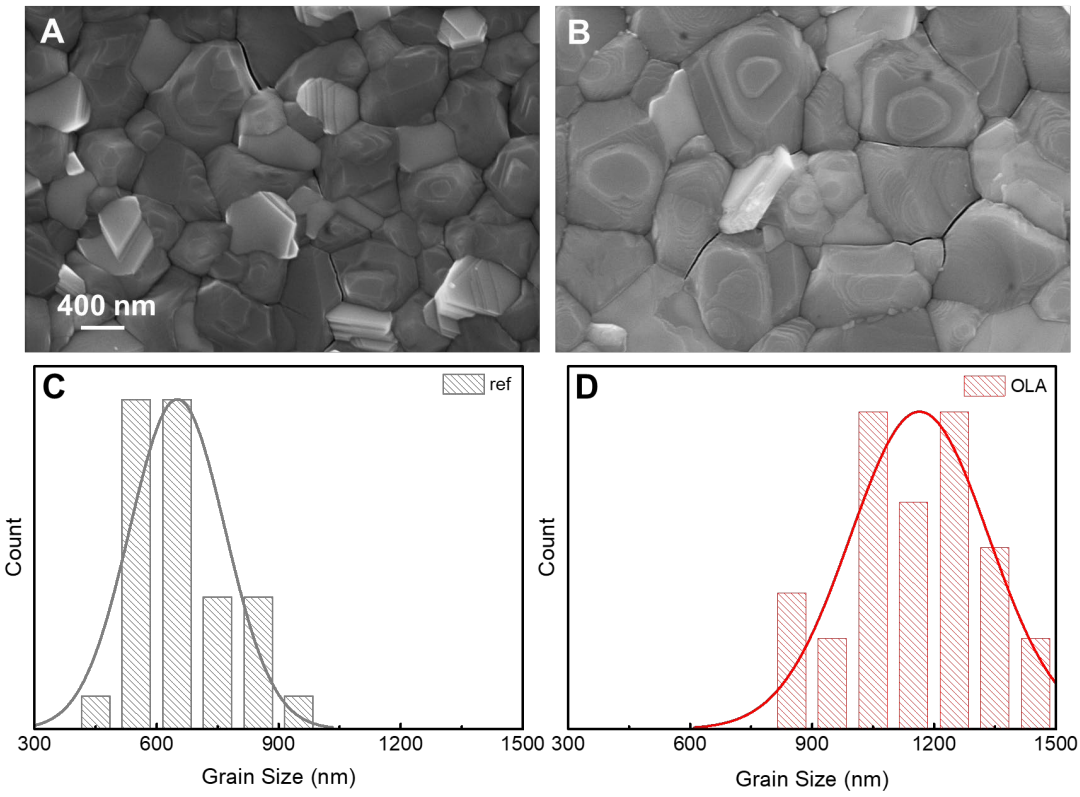

Fig. S11 SEM image of FA-based perovskite films (A) without and (B) with OLA treatment. Grain size statistical distribution of FA-based perovskite films (C) without and (D) with OLA treatment.

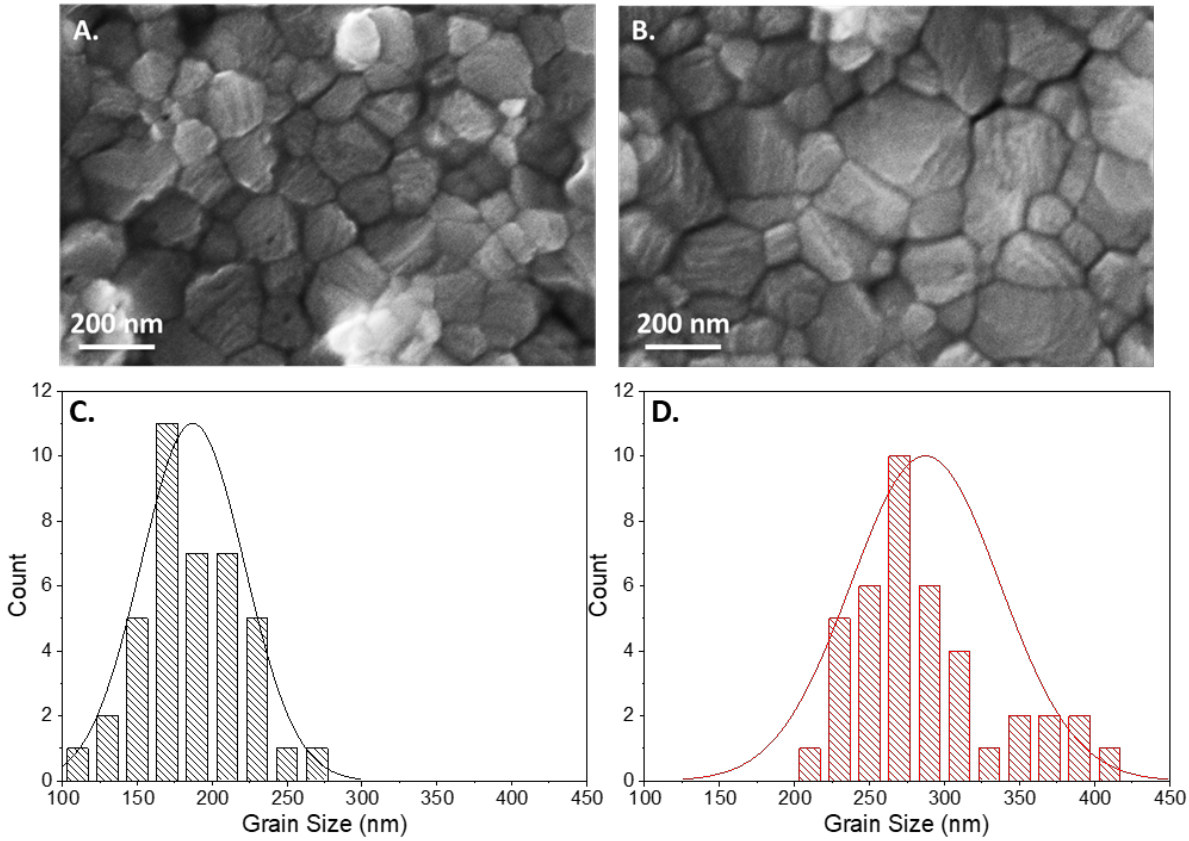

Fig. S12. SEM image of MA-based perovskite films (A) without and (B) with OLA treatment. Grain size statistical distribution of MA-based perovskite films (C) without and (D) with OLA treatment.

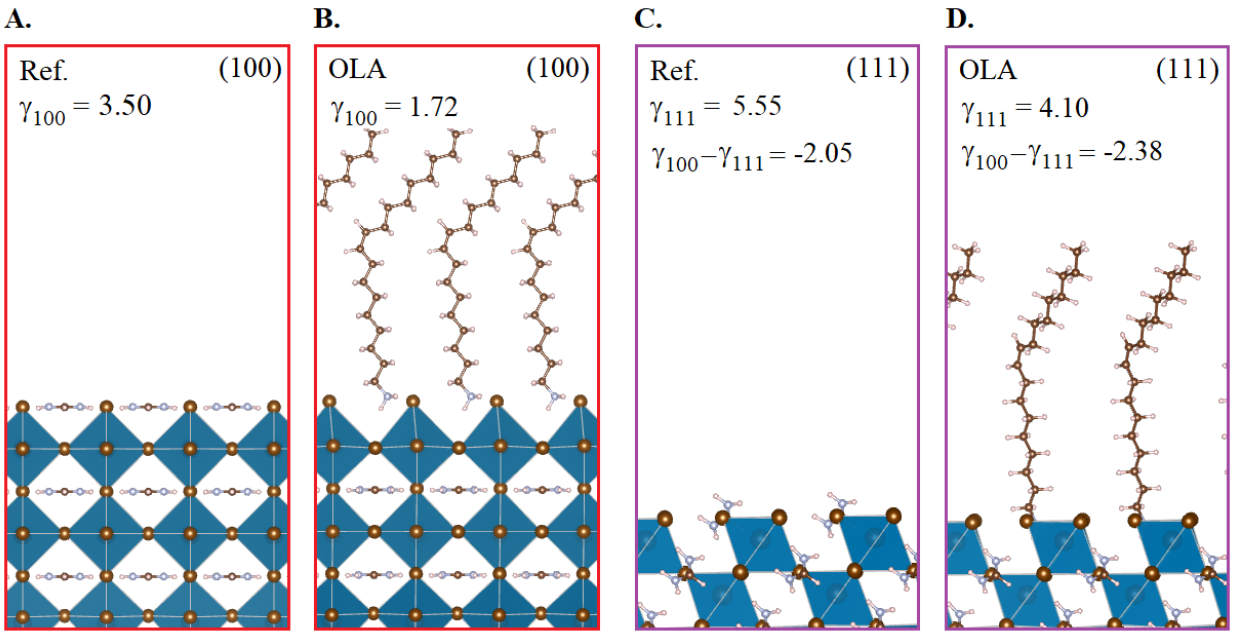

Fig. S13. DFT-D3 calculated surface energies, γ, of 100 and 111 slabs of $FAPbI_3$, with and without OLA treatment. (A) 100 slab without OLA, (B) 100 slab with OLA, (C) 111 slab without OLA and (D) 111 slab with OLA. The surface energies are in eV/nm^2 units.

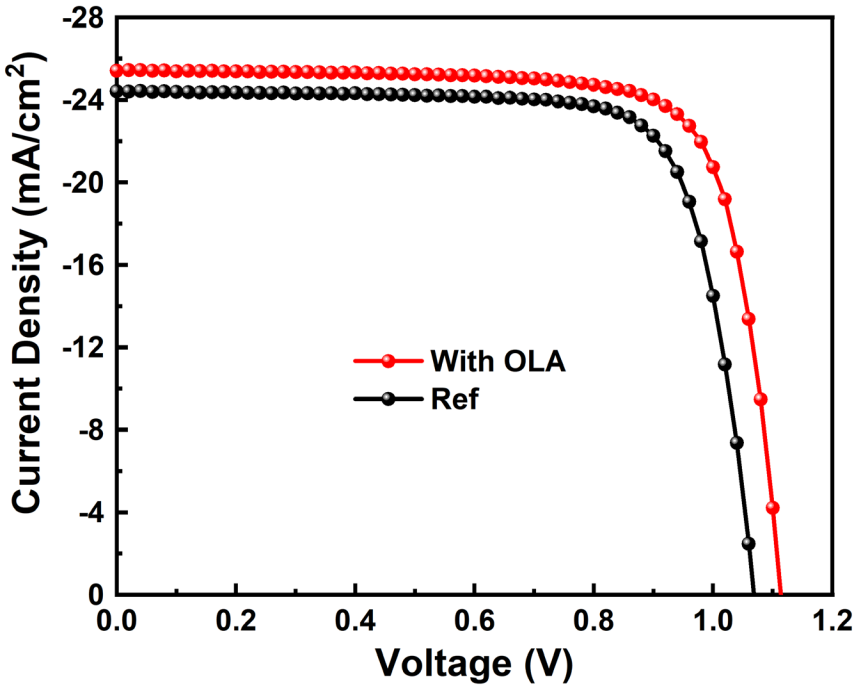

Fig. S14. *J-V* curves of devices under simulated one-sun AM1.5G illumination with and without OLA treatment. (Ref: V_{oc}=1.069 V, J_{sc}=24.41 mA/cm^2, FF=76.81%, PCE=20.04%; OLA: V_{oc}=1.113 V, J_{sc}=25.40 mA/cm^2, FF=78.19%, PCE=22.13%).

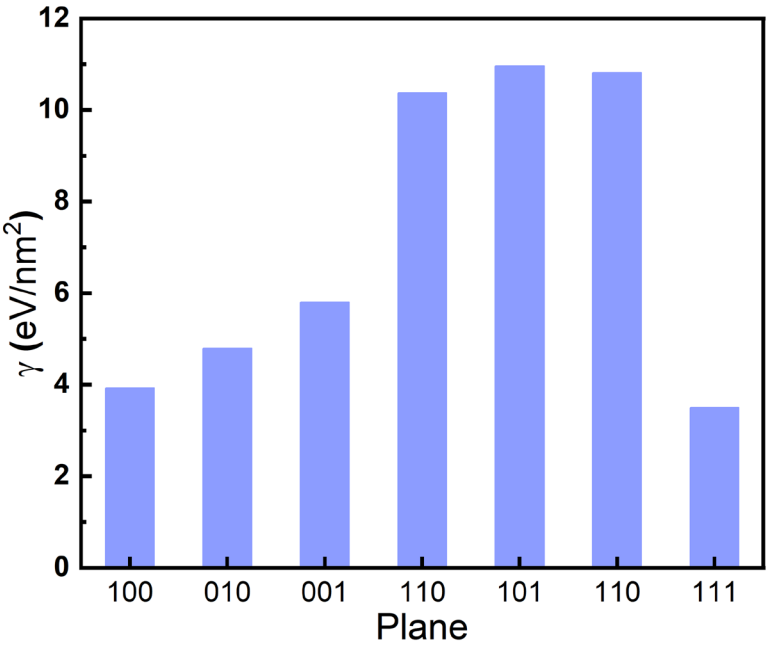

Fig. S15 DFT-D3 calculated γ^{clean} for various slabs of $CsPbI_2Br$.

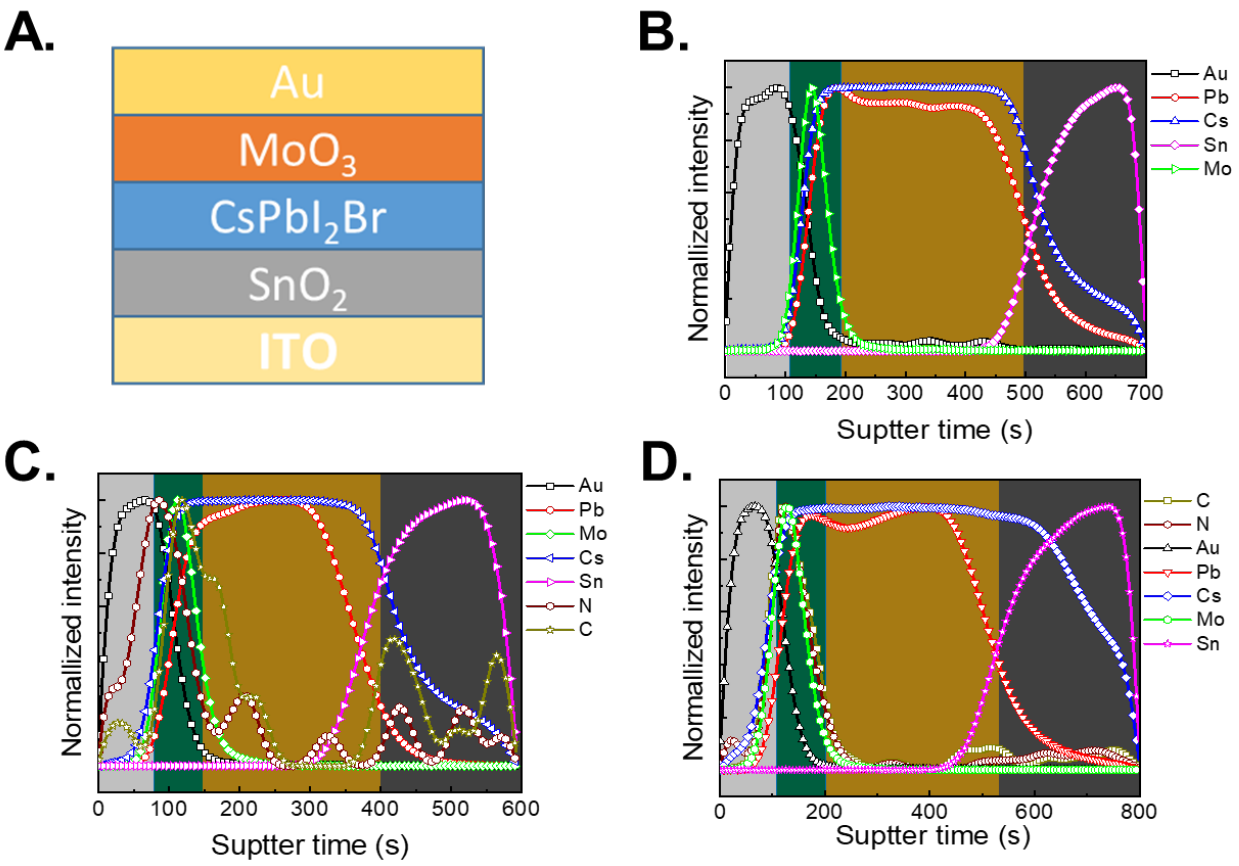

Fig. S16. Spatial distribution of other organic ammoniums in perovskite devices. (A) The configuration of device measured in TOF-SIMS. (B) Spatial distribution of pure perovskite device. (C) Spatial distribution of BA-treated perovskite device. (D) Spatial distribution of OCA-treated perovskite device.

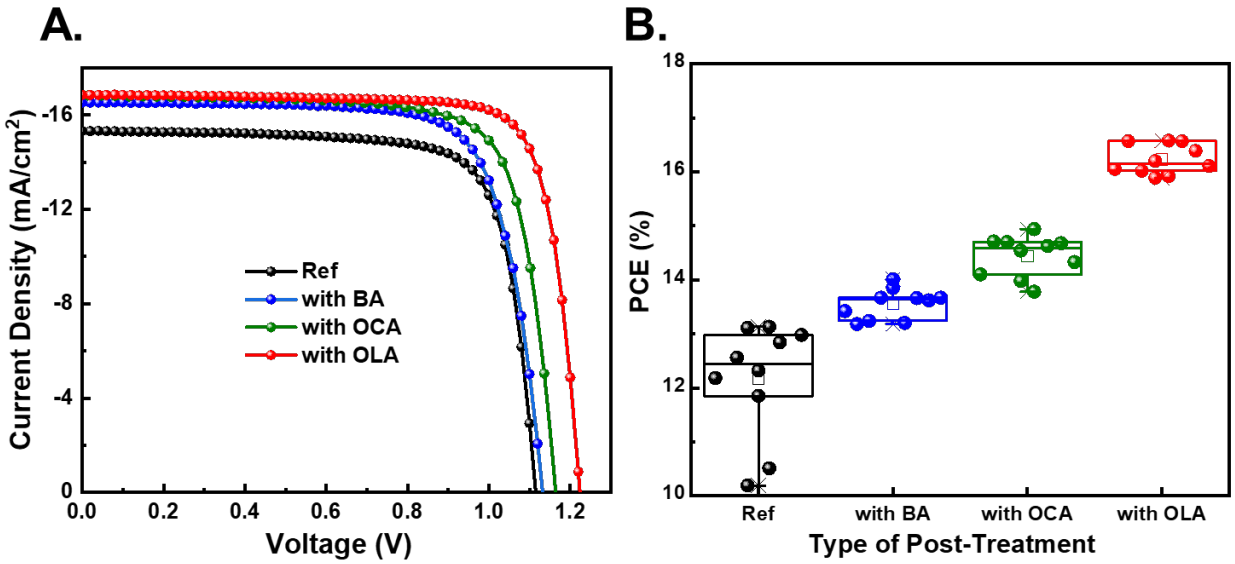

Fig. S17 (A) *J-V* curves of devices under simulated one-sun AM1.5G illumination with or without organic ammonium treatments. (B) Statistical distribution of device PCEs of under simulated one-sun AM1.5G illumination with or without organic ammonium treatments.

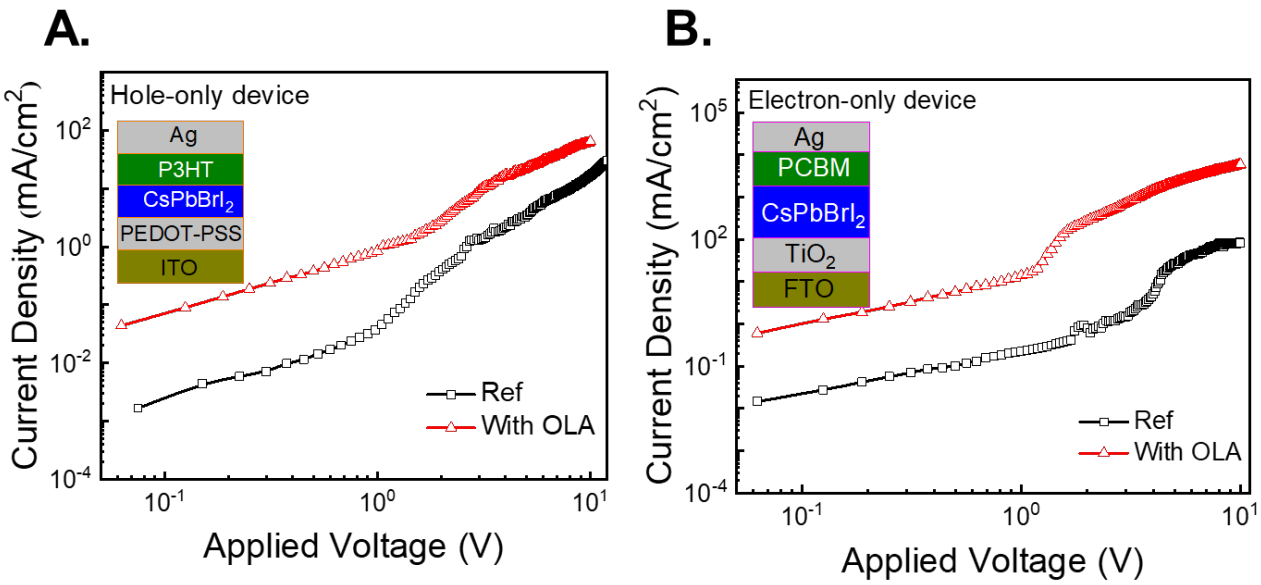

Fig. S18. Electron and hole mobility of devices (A) with or (B) without OLA treatment measured by space charged limited current (SCLC).

Table S1 Calculated surface energies based on DFT-D3 method. Ref. refers to the case where Cs^+ cations are present in the top layer, whereas they are replaced by BA, OCA and OLA for the remaining cases.

Type of Treatment	γ_{100} (eV/nm^2)	γ_{111} (eV/nm^2)	δ (eV)
Ref.	4.33	4.03	+0.29
BA	3.23	4.09	-0.87
OCA	2.14	4.06	-1.92
OLA	1.71	4.01	-1.96

Table S2. The contact angles of H_2O and DIM on $CsPbI_2Br$ with or without OLA treatment and their respective calculated surface free energies.

i	H_2O (°)	DIM (°)	γ_s [mN m^{-1}]
Ref	46.3	7.4	59.78
OLA	76.1	46.3	38.38

Table S3 Surface formula, number of formula per unit cell and atomic energy term that enter γ^{clean} for the calculation of surface energies at $T = 0$ K. n is the number of formula units per unit cell.

Slab	Formula	n	$2A * \gamma^{clean} + nE^{bulk} - E^{slab}$
100	$Cs_nPb_nI_{2n+1}Br$	3	$-E_I$
010	$Cs_nPb_nI_{2n+1}Br$	3	$-E_I$
001	$Cs_nPb_nI_{2n}Br_{n+1}$	3	$-E_{Br}$
110	$Cs_{n-1}Pb_nI_{2n}Br_n$	4	E_{Cs}
101	$Cs_{n-1}Pb_nI_{2n}Br_n$	4	E_{Cs}
011	$Cs_{n-1}Pb_nI_{2n}Br_n$	4	E_{Cs}
111	$Cs_{n-1}Pb_nI_{2n}Br_n$	8	E_{Cs}

Table S4. Average and the best device data based on $CsPbI_2Br$ treated with or without various types of organic ammoniums.

Type of Treatment	V_{OC} (V)	J_{SC} (mA cm^{-2})	FF (%)	PCE (%)	
				average	best
Ref	1.103±0.02	15.15±0.25	0.73±0.05	12.17±1.05	13.13
BA	1.137±0.01	15.96±0.46	0.75±0.03	13.55±0.28	14.01
OCA	1.166±0.02	16.29±0.25	0.76±0.01	14.44±0.38	14.94
OLA	1.231±0.01	16.48±0.26	0.80±0.01	16.23±0.28	16.58

Table S5. Average and the best device data based on $CsPbI_2Br$ treated with OLA using different annealing temperatures.

Anneal Temperature (°C)	V_{OC} (V)	J_{SC} (mA cm^{-2})	FF (%)	PCE (%)	
				average	best
75	1.213±0.02	16.15±0.25	0.78±0.01	15.28±0.34	15.65
100	1.231±0.01	16.48±0.26	0.80±0.01	16.23±0.28	16.58
125	1.221±0.01	16.18±0.25	0.78±0.01	15.38±0.27	15.61
150	1.211±0.01	16.07±0.21	0.77±0.01	14.97±0.31	15.39

Table S6. Average and the best device data based on $CsPbI_2Br$ treated with OLA using different annealing time.

Anneal Time (min)	V_{OC} (V)	J_{SC} (mA cm^{-2})	FF (%)	PCE (%)	
				average	best
3	1.222±0.01	16.19±0.28	0.79±0.01	15.63±0.28	16.06
5	1.231±0.01	16.48±0.26	0.80±0.01	16.23±0.28	16.58
10	1.243±0.01	16.24±0.34	0.75±0.01	15.14±0.33	15.52
20	1.247±0.01	15.92±0.43	0.73±0.01	14.49±0.28	14.83

Table S7. Average and the best device data based on $CsPbI_2Br$ treated with OLA using different concentrations.

OLA Concentration (mg/ml)	V_{OC} (V)	J_{SC} (mA cm^{-2})	FF (%)	PCE (%)	
				average	best
0.5	1.204±0.01	16.25±0.19	0.76±0.01	14.87±0.34	15.22
1	1.231±0.01	16.48±0.26	0.80±0.01	16.23±0.28	16.58
2	1.242±0.01	16.20±0.21	0.73±0.01	14.69±0.27	15.01

Table S8. Hole and electron mobilities of devices based on $CsPbI_2Br$ treated with or without OLA.

Type of Treatment	μ_h ($cm^2 V^{-1} s^{-1}$)	μ_e ($cm^2 V^{-1} s^{-1}$)
Ref	2.6×10^{-3}	1.0×10^{-2}
OLA	2.7×10^{-2}	5.7×10^{-1}

References

(1) G. Kresse, J. Furthmüller, *Comput. Mater. Sci.* **1996**, 6, 15–50.
(2) G. Kresse, J. Furthmüller, *Phys. Rev. B - Condens. Matter Mater. Phys.* **1996**, 54, 11169–11186.
(3) J. P. Perdew, K. Burke, M. Ernzerhof, *Phys. Rev. Lett.* **1996**, 77, 3865–3868.
(4) J. P. Perdew *et al.*, *Phys. Rev. B*. 1992, 46, 6671–6687.
(5) S. Grimme, J. Antony, S. Ehrlich, H. Krieg, *J. Chem. Phys.* **2010**, 132, 154104.
(6) S. Grimme, S. Ehrlich, L. Goerigk, *J. Comput. Chem.* **2011**, 32, 1456–1465.
(7) D. Joubert, *Phys. Rev. B - Condens. Matter Mater. Phys.* 1999, 59, 1758–1775 (1999).
(8) H. J. Monkhorst, J. D. Pack, *Phys. Rev. B*. **1967**, 13, 5188–5192.
(9) P. N. Abufager *et al.*, *Phys. Chem. Chem. Phys.* **2011**, 13, 9353–9362 (2011).
(10) I. Steinbach. *Modelling Simul. Mater. Sci. Eng.* **2009**, 17, 073001.
(11) OpenPhase. URL http://www.openphase.de
(12) H. Zhao *et al.*, *Adv. Mater.* **2018**, 30, 1805041.